

# FIRST SYNOPTIC MAPS OF PHOTOSPHERIC VECTOR MAGNETIC FIELD FROM SOLIS/VSM: NON-RADIAL MAGNETIC FIELDS AND HEMISPHERIC PATTERN OF HELICITY

S. GOSAIN<sup>1</sup> A. A. PEVTSOV<sup>1</sup> G. V. RUDENKO<sup>2</sup> AND S. A. ANFINOGENTOV<sup>2</sup>

*To appear in ApJ*

## ABSTRACT

We use daily full-disk vector magnetograms from Vector Spectromagnetograph (VSM) on Synoptic Optical Long-term Investigations of the Sun (SOLIS) system to synthesize the first Carrington maps of the photospheric vector magnetic field. We describe these maps and make a comparison of observed radial field with the radial field estimate from LOS magnetograms. Further, we employ these maps to study the hemispheric pattern of current helicity density,  $H_c$ , during the rising phase of the solar cycle 24. Longitudinal average over the 23 consecutive solar rotations shows a clear signature of the hemispheric helicity rule, i.e.  $H_c$  is predominantly negative in the North and positive in South. Although our data include the early phase of cycle 24, there appears no evidence for a possible (systematic) reversal of the hemispheric helicity rule at the beginning of cycle as predicted by some dynamo models. Further, we compute the hemispheric pattern in active region latitudes ( $-30^\circ \leq \theta \leq 30^\circ$ ) separately for weak ( $100 < |B_r| < 500$  G) and strong ( $|B_r| > 1000$  G) radial magnetic fields. We find that while the current helicity of strong fields follows the well-known hemispheric rule (i.e.,  $\theta \cdot H_c < 0$ ),  $H_c$  of weak fields exhibits an inverse hemispheric behavior (i.e.,  $\theta \cdot H_c > 0$ ) albeit with large statistical scatter. We discuss two plausible scenarios to explain the opposite hemispheric trend of helicity in weak and strong field region.

*Subject headings:* Sun: Flares, Sunspots, magnetic field, helicity

## 1. INTRODUCTION

Solar magnetic fields exhibit a hemispheric preference in their sense of twist or helicity. Using chromospheric  $H_\alpha$  images Hale (1927) studied super-penumbral whirls around sunspots. He found that similar to terrestrial hurricanes, sunspot whirls exhibit hemispheric preference in their shape. Later, Richardson (1941) verified results of Hale (1927) by studying a larger data set and found a hemispheric preference at  $\sim 70\%$  level, although only about one-third of the sunspots showed  $H_\alpha$  vortices. Origin of twist in super-penumbral whirls, initially believed to be due to Coriolis force acting on plasma flows, is now attributed to presence of electric currents in sunspot magnetic fields. Later studies establish what is now known as the hemispheric helicity rule in various solar features associated with magnetic fields: chromospheric filaments (Rust 1999; Martin et al. 2008), super-penumbral whirls (Balasubramanian et al. 2004), sheared coronal arcades (Rust & Kumar 1996; Canfield et al. 1997), and interplanetary magnetic field (Smith 1999).

Observations from modern vector magnetographs enabled researchers to carry out a quantitative study of magnetic/current helicity and its sign (chirality) (Seehafer 1990; Pevtsov et al. 1995; Abramenko et al. 1996). The chirality from magnetograms is deduced by deriving the quantity,  $\alpha = (\nabla \times \vec{B})_z / B_z = J_z / B_z$ , where  $J_z$  is the vertical component of electric current density. This parameter  $\alpha$  is also known as the force-free parameter following the definition of force-free fields for which

the Lorentz force is zero, i.e.,  $\vec{J} \times \vec{B} = 0$ , which in turn implies  $\vec{J} = \nabla \times \vec{B} = \alpha \vec{B}$ . Although the gas pressure and magnetic pressure are comparable at photosphere and so photospheric fields are not completely force-free (Priest 1984; Metcalf et al. 1995), such approximations are widely used to extrapolate magnetic fields in the corona using photospheric magnetic field measurements. The observations show a hemispheric preference for the sign of  $\alpha$  parameter in solar active regions with preferentially negative values in the North and positive values in the Southern hemisphere (Seehafer 1990; Pevtsov et al. 1995; Longcope et al. 1998). Similar results are obtained by analyzing the vertical component of current helicity density  $H_c^z$ , or simply  $H_c$ , given by  $H_c = J_z \cdot B_z$ , whose sign measures the sense of twist of the magnetic field (Abramenko et al. 1996; Bao & Zhang 1998). Here one must bear in mind that only vertical component of current helicity density is measured from vector magnetograms observed at a single height, the other two components can in principle change the sign of true current helicity density. However, under the assumption that the sense of flow (parallel or antiparallel) of the vertical component of electric current,  $J_z$ , with respect to  $B_z$ , is same as that of current vector  $\vec{J}$  along  $\vec{B}$ , we can treat the vertical component of current helicity density as a measure of twist. Seehafer (1990) showed that for cylindrically symmetric flux tube magnetic and current helicity have same sign and increase with each other. Further, it can be shown that  $\alpha$  and  $H_c$  are related to each other:  $H_c = \alpha B_z^2$  (Hagyard & Pevtsov 1999).

The hemispheric helicity rule is also present in large scale magnetic fields (LSMF) (Pevtsov & Latushko 2000; Wang & Zhang 2010). In full sun MHD simulations, Yeates et al. (2008) found similar hemispheric preference but only at mid/low latitudes. At higher lati-

<sup>1</sup> National Solar Observatory, 950 N Cherry Avenue, Tucson 85719, Arizona, USA

<sup>2</sup> Institute of Solar-Terrestrial Physics (ISTP), Russian Academy of Sciences, Irkutsk, Russia

tudes they found a reversal of the hemispheric pattern of twist, which is in contrast to the observations which show that polar crown filaments having chirality preference of the same nature as active regions. In addition to the hemispheric helicity rule, the helicity of LSMF was found to show evidence of zonal organized bands (Pevtsov & Balasubramaniam 2003) co-spatial with patterns of torsional oscillations (Howe et al. 2000). Sign of helicity in these bands is opposite to  $H_c$  prevailing for a given hemisphere.

Until recently, the full disk vector magnetograms were not routinely available, and thus, early studies of  $H_c$  in large-scale fields were based on pseudo-vector derivations. In this method, the components of LSMF vector are derived from time sequence of longitudinal magnetograms under the simple assumption that the field does not change over several days. Even with this assumption, the derivations are limited to only two components (radial and toroidal), the variation in projection are too small to derive the meridional component of the field (however, see Wang & Zhang (2010)). The routine observations of full disk vector magnetic fields by Vector Spectromagnetograph (VSM) on Synoptic Optical Long-term Investigations of the Sun (SOLIS) system (Keller et al. 2003) and Helioseismic Magnetic Imager (HMI) (Schou et al. 2012) on Solar Dynamic Observatory (SDO) spacecraft, allow for the first time to investigate the current helicity of large-scale magnetic field directly without any restrictive assumptions about the nature of these fields.

In this paper we present the first ever synoptic Carrington maps of the vector magnetic field constructed from VSM/SOLIS daily observations. We contrast the new maps with traditional Carrington charts derived from longitudinal field measurements and find significant differences between true and LOS-based radial magnetic field in areas of active regions and at high latitudes. In Section 2 we briefly describe the SOLIS/VSM instrument and the method of deriving the full disk vector magnetograms. Then we describe synoptic maps of vector magnetic field and the properties of the radial magnetic field in Sections 3 and 4. In Section 5 we present the analysis of the current helicity density based on new synoptic maps. In Section 6 we study the helicity pattern in strong and weak magnetic field regions separately, and in Section 7 we discuss our findings.

## 2. OBSERVATIONS AND DATA ANALYSIS

We employ daily observations of vector magnetic fields taken with the Vector Spectromagnetograph (VSM)- one of three instruments comprising SOLIS facility for synoptic observations of the Sun in optical wavelengths (Keller et al. 2003; Balasubramaniam & Pevtsov 2011).

SOLIS/VSM is spectrograph-based spectropolarimeter. It takes the full Stokes profiles of the Fe I 630.15 – 630.25 nm line pair along slightly curved spectrograph slit that intersects the entire solar disk (from East to West limbs). Full disk magnetogram is built by scanning the solar image by moving the telescope in the declination. Pixel size in final magnetogram is about  $1 \times 1$  arcsec<sup>2</sup>. VSM takes about 0.6 seconds to record all four Stokes parameters for a single scan line, and it takes about 20 minutes to complete a full disk magnetogram (2048 scan lines).

The Stokes I, Q, U, and V profiles observed in Fe I 630.15-630.25 nm line pair are sampled in spectral direction with  $2.4 \text{ pm pixel}^{-1}$ . The spectra are inverted in a framework of Milne-Eddington model of stellar atmosphere following Unno-Rachkovsky formalism (Skumanich & Lites 1987).

Additional details about the instrument and the pipeline reduction steps can be found elsewhere (e.g., (Jones et al. 2002; Henney et al. 2006; Balasubramaniam & Pevtsov 2011)). Only pixels with polarization signal above the threshold of 0.1% of continuum intensity,  $I_c$ , are inverted to obtain the magnetic (field strength, inclination angle and azimuth angle) and thermodynamic (e.g., Doppler width, Doppler velocity, source function, temperature) parameters. The method also allows to determine the relative contribution of magnetic and non-magnetic plasma to line profile for each pixel (filling factor). The threshold of 0.1% of  $I_c$  corresponds to typical noise level in the continuum. Using this threshold avoids fitting profiles buried in the noise. The error in inferred magnetic field parameter for each pixel is different as Stokes signal varies from pixel to pixel. For example, Gosain et al. (2010) used *Hinode* vector magnetogram of a sunspot region as reference field and simulated random errors due to normally distributed photometric noise (0.5% of  $I_c$ , a  $3\text{-}\sigma$  noise level) in Stokes profiles and found that maximum error in the magnetic field parameters is  $\sim 50 \text{ G}$  for field strength,  $\sim 1.5^\circ$  for inclination and  $\sim 5^\circ$  for azimuth angle, respectively. Stokes profiles in regions like sunspots, plage, network and decaying regions have typically SNR  $\geq 1000$  and so the typical errors are expected to be in this range. The noise levels in SOLIS magnetograms are estimated to be a few Gauss in the longitudinal and 70G in the transverse field measurements (Tadesse et al. 2013).

The 180 degrees azimuth ambiguity is resolved using Non-Potential Field Computation (NPFC) method (Georgoulis 2005; Georgoulis et al. 2008). Due to limited memory and CPU speed constrains in early data reduction pipe-line hardware, the 180-degree disambiguation is parallelized by dividing the solar image into smaller overlapping tiles. The azimuth ambiguity is resolved in each tile independently. For this study, we have also tested a new faster ambiguity resolution method developed by Rudenko & Anfinogentov (2011). In this method, the direction of the transverse field is determined in accordance with the principle of minimum deviation of net differences of the potential field from those of the defined field. The results presented in this paper are found to be same with both ambiguity resolution algorithms, which tests the validity and consistency of the new and faster algorithm developed by Rudenko & Anfinogentov (2011).

## 3. SYNOPTIC MAPS OF THE MAGNETIC FIELD VECTOR

To compute helicity of magnetic fields over the entire solar disk requires constructing the synoptic maps of vector field. Until now, no such maps were produced. Here we describe our approach to constructing the vector field synoptic maps and compare these new maps with traditional synoptic maps of radial field, which are created from LOS magnetograms under a restrictive assumption that magnetic field are normal to solar surface.

Traditionally, synoptic (or Carrington) maps are synthesized by combining the daily full-disk magnetograms taken over the period of one solar rotation ( $\approx 27$  days). The maps cover all latitudes ( $\pm 90$  degrees) and longitudes (0–360 degrees) of solar surface. Although the purpose of synoptic map is to represent activity over entire surface of the Sun, the maps are representative of the activity occurring near the central meridian (CM) of the solar disk at the time of observations. In earlier times when the angular resolution of data was coarse a  $\cos^4\phi$  weighting was used (Harvey et al. 1980), where  $\phi$  is the longitudinal distance from the central meridian. With the availability of higher-resolution data, it has been found that such weighting leads to a smearing of small scale features which evolve substantially from day to day. A Gaussian weighting scheme of the form  $W(\phi) = \exp^{-(\phi/\tau)^2}$  has therefore been implemented (J. W. Harvey, private communication) in order to heavily weight only the regions very close to the CM. Such synoptic maps, therefore, essentially capture a snapshot of activity very close to the CM over the duration of solar rotation.

Synoptic maps based on the LOS magnetic field of the Sun are widely used to study the evolution of magnetic fields on time scales from solar rotation to the solar cycle. The maps of radial field, constructed from LOS magnetograms are used as the lower boundary condition for extrapolating the photospheric fields into the corona in a framework of potential field extrapolation (Altschuler & Newkirk 1969). The current-free fields extrapolated to the heights in the corona where they deemed to become purely radial (Potential Field Source Surface, or PFSS, typically between 2.5 and 3.5  $R_\odot$ ) are used in modeling the coronal and heliospheric magnetic fields, the solar wind speed and the appearance of white-light corona prior to total solar eclipses. The validity of the assumption that the magnetic field is normal to the surface at the photosphere level is largely unknown. Thus, the availability of synoptic maps of vector magnetic field allows us to verify the assumption of field verticality for the first time.

Below we describe the steps taken in constructing the vector synoptic maps.

- After the 180-degree ambiguity is resolved, the three components of the field in image plane ( $B_x$  - (terrestrial) East-West direction,  $B_y$  - (terrestrial) North-South component, and  $B_z$  - vertical) are transformed to heliographic coordinate system which yields toroidal ( $B_\phi$ ), poloidal ( $B_\theta$ ) and radial ( $B_r$ ) component. The full-disk magnetograms are then re-mapped into heliographic coordinates (longitude:  $\phi$ , latitude:  $\theta$ ).
- The individual re-mapped magnetograms are combined in traditional way with a Gaussian weight of the form  $W(\phi) = \exp^{-(\phi/\tau)^2}$  given to the data. This results in three synoptic maps (one for each component of vector field) corresponding to one Carrington rotation.

As an example, in Figure 1 we show a vector synoptic map for Carrington rotation 2109. The zoom-in of a typical active region (Box ‘1’) and a diffuse bipolar

region (Box ‘2’) along with the overlaid transverse vector is shown in the Figure 2. We find the active region field pattern to be consistent with expectation for dipolar field configuration:  $B_\phi$  component (Box ‘1’) between two polarities corresponds to field lines connecting them, and  $B_\theta$  is in agreement with the group tilt corresponding to Joy’s law (Hale et al. 1919). The patterns for large scale field (Box ‘2’) are similar to those obtained by Pevtsov & Latushko (2000) with the pseudo-vector method for their data during cycle 22. Both foot points of the field in Box ‘2’ show negative  $B_\phi$ , which means that the field lines are connected such that the foot points make obtuse angle with solar surface, measured from polarity inversion line (PIL). Further, the transverse field vectors in diffuse bipolar region (Box ‘2’) show a North-South component ( $B_\theta$ ) such that the field configuration is tilted towards equator. The reason for the equator-ward tilt could be presence of a filament along the PIL would suggest a non-potential field oriented along the PIL, which is oriented roughly along N-S direction. Further, the period of this observation (29-April-2011) corresponds to ascending phase of solar cycle 24, so coronal equatorial streamers which are prominent during solar minima, may also give the large scale field (reaching high in the corona), a net equator-ward tilt. Thus, the derived components of vector magnetic field in our synoptic maps agree with the expected orientation of magnetic fields on the Sun.

#### 4. OBSERVED RADIAL FIELD VERSUS RADIAL FIELD ESTIMATE FROM LONGITUDINAL MAGNETOGRAMS

Assuming that the magnetic field on the Sun is mostly vertical, one can estimate the radial field,  $B_{r(LOS)}$ , using the relation  $B_{r(LOS)} = B_{LOS}/\mu$ , where  $\mu$  is the cosine of the heliocentric angle and  $B_{LOS}$  is the line-of-sight field. Traditional synoptic maps of radial field are synthesized using this method, which will work exactly if the field were truly normal to the solar surface. However, in practice magnetic fields are not normal everywhere. For example, the fields are more horizontal in sunspot penumbra and near PIL. Although, in most cases the field in quiet Sun appears to be more vertical, it is not purely normal to the solar surface (Gosain & Pevtsov 2012). The departure of high latitude fields from radial expansion at the photospheric level was deduced using vector field reconstructed from longitudinal magnetograms by Petrie & Patrikeeva (2009).

Now let us compare the radial field reconstructed from longitudinal measurements,  $B_{r(LOS)}$ , with the observed radial field component from vector field measurements,  $B_{r(OBS)}$  (or simply  $B_r$ , for brevity). For comparison we compute the difference of the absolute value of two radial fields, i.e.,  $\Delta B_r = |B_r| - |B_{r(LOS)}|$ , and plot signed relative difference,  $\Delta B_r/|B_r|$  (%), as shown in the top panel of Figure 3. This signed difference map is saturated at  $\pm 5\%$  to emphasize the latitudinal pattern in the sign of the difference. Black (white) correspond to negative (positive) difference, i.e.,  $|B_r| < |B_{r(LOS)}|$  and  $|B_r| > |B_{r(LOS)}|$ , respectively. It can be noticed that in active regions the differences are large as compared to fields outside active regions at that latitudes. This is expected due to the presence of fanning fields in active regions.

Further, in the middle panel of Figure 3 we show the longitudinal average of absolute value of relative dif-

ference,  $|\Delta B_r|/|B_r|$  (in %). One can notice that the value of relative difference increases systematically towards higher latitudes. The observations are scanty at higher latitudes, hence a large scatter is seen, but the systematic increase towards higher latitudes is evident from the profile. To understand the cause of this systematic increase let us consider a field of strength  $B$  at latitude  $\theta$  having an inclination  $\pm\gamma$  in the meridional plane with respect to local vertical. The positive or negative sign corresponds to case when the field is inclined towards poles or solar equator. Then the LOS field,  $B_L$  and radial field,  $B_r$  would be given by

$$\begin{aligned} B_L &= B \cdot \cos(\theta \pm \gamma) \\ B_r &= B \cdot \cos(\gamma) \end{aligned}$$

When the assumption is made that the field is normal to the solar surface ( $\gamma = 0$ ),  $B_r(LOS)$  is derived as  $B_L/\cos(\theta) = B\cos(\theta \pm 0)/\cos(\theta)$ . But if the field is not vertical ( $\gamma \neq 0$ ), this assumption introduces an error. In the latter case,  $B_r(LOS) = B\cos(\theta \pm \gamma)/\cos(\theta)$ .

Difference ( $\Delta B_r$ ) between true  $B_r$  and one derived from assumption that field is vertical can be expressed as following:

$$\frac{\Delta B_r}{B_r} = 1 - \frac{\cos(\theta \pm \gamma)}{\cos(\theta)\cos(\gamma)}$$

One can show that

$$\frac{\Delta B_r}{B_r} = \frac{\Delta B_r}{|B_r|} = \pm \tan(\theta)\tan(\gamma)$$

The expression for normalized amplitudes of difference between true  $B_r$  and  $B_r(LOS)$  becomes

$$\frac{|\Delta B_r|}{|B_r|} = \tan(\theta)\tan(\gamma)$$

Thus, even if  $\gamma =$  constant,  $|\Delta B_r|/|B_r|$  will vary as tangent of latitude ( $\theta$ ). The profile in middle panel of Figure 3 demonstrates that the effects of non-verticality of magnetic field become stronger (and more important) for high latitudes even if the inclination angle does not change systematically.

Further, it can be noticed that there is a systematic pattern in the sign of the relative difference,  $\Delta B_r/|B_r|$ , as described below.

- Both the active regions as well as the diffuse field outside active regions show asymmetry in the sign of  $\Delta B_r/|B_r|$  along the North-South direction.
- In both hemispheres, the portion of the active region towards the equator (pole) shows negative (positive) values of  $\Delta B_r/|B_r|$ .
- Outside active regions the diffuse flux in both hemispheres shows opposite pattern as compared to active regions, i.e., the flux near the equator (pole) shows positive (negative) value of  $\Delta B_r/|B_r|$ .

Negative  $\Delta B_r/|B_r|$  in high latitudes in Northern and Southern hemispheres implies a systematic tilt of vector magnetic fields towards equator. The bottom panel of Figure 3 illustrates a cartoon of the side view of portion of the solar disk visible to observer (labeled LOS) and

some example field lines (dashed curved lines). The labels correspond respectively as follows: North Pole:NP, South Pole:SP, Equator: EQ, Radial Direction: R, Center of Sun: O, Active Region: AR, Low Latitude: LL, and High Latitude: HL. It can be seen that in active region (labeled AR), depicted like a sunspot with the field lines fanning out, the equator-ward portion of AR will have field lines oriented in such a way that they deviate from local solar vertical, inclining towards the equator. Similarly the pole-ward portion of AR will have field lines oriented in such a way that they deviate from local solar vertical, inclining towards poles. Then the field inclined towards equator (pole) will show negative (positive) sign of  $\Delta B_r/|B_r|$ , which is what we observe in top panel of Figure 3. On the other hand the large scale field lines (depicted by dashed curved lines) rooted in HL and LL deviate from local solar vertical inclining equator-ward and pole-ward, respectively. Thus, we will see  $\Delta B_r/|B_r|$  to be negative in HL regions and positive in LL regions, which is what we observe in top panel of Figure 3.

These results emphasize importance of vector field measurements. The quantitative effects arising from replacing the  $B_r(LOS)$  synoptic maps by observed  $B_r$  on solar wind and coronal field extrapolation are unknown. These effects and detailed study of non-radial nature of fields will be a subject to our separate future study. Here we want to emphasize the importance of vector field measurements and the synoptic maps in deriving the  $B_r$ , and potentially calibrate the systematic deviation  $\Delta B_r/|B_r|$  with latitude.

The systematic pattern shown in top panel of Figure 3 cannot be a result of random noise. In Appendix-A we show that the random noise in  $B_r$  and  $B_r(LOS)$  will lead to random noise in relative difference and not a systematic variation in its sign as shown in top panel of Figure 3.

## 5. CURRENT HELICITY DENSITY FROM SYNOPTIC VECTOR MAPS

Given the distribution of vector magnetic field in the photosphere one can compute the vertical component of current helicity density,  $H_c$ . In spherical coordinates

$$\begin{aligned} H_c(\phi, \theta) &= B_r(\nabla \times \vec{B})_r \\ &= \frac{1}{\sin\theta} \left\{ \frac{\partial}{\partial\theta} [\sin\theta B_\phi(\phi, \theta)] - \frac{\partial B_\theta(\phi, \theta)}{\partial\phi} \right\} B_r(\phi, \theta) \end{aligned}$$

The distribution of  $H_c$  for Carrington rotation (CR) 2109 is shown in Figure 4. The patterns of current helicity density of mixed sign can be seen in the active region. Such local helicity patterns are well known from previous works (e.g. Pevtsov & Peregud 1990; Pevtsov et al. 1994; Abramenko et al. 1996; Pevtsov & Canfield 1998; Su et al. 2009, and references therein).

In the present work we computed maps of vertical component of current helicity density for CR 2109 to 2131 covering a period from March 2011 to December 2012. During this time a total of 453 NOAA numbered active regions crossed the solar disk. The longitudinal average of  $H_c$ , or  $\langle H_c \rangle$ , distribution over all the CR is shown in top panel of Figure 5. The  $\langle H_c \rangle$  profile shows a tendency to be positive in Southern and negative in Northern hemisphere of the Sun, in agreement with the previous results obtained by many researchers

for active regions observed in cycles 22, 23 and even 24 (Abramenko et al. 1996; Bao et al. 2000; Pevtsov et al. 2001; Hao & Zhang 2011).

In Figure 5, the  $H_c$  is averaged over regular ARs, ephemeral regions, large scale bipolar and unipolar magnetic regions and plages up to high latitudes ( $\sim 60^\circ$ ). In the lower panel of Figure 5 we show the data points confined to active region belt ( $0-30^\circ$ ) and we fit a straight line to the observed data points to show that the slope of  $dH_c/d\theta$  is negative, indicative of hemispheric sign preference. In computing the average profiles of  $H_c$  we used only the pixels above the threshold of 20 G for both radial and transverse fields to filter out the noise.

In the left panel of Figure 6 we construct the time-latitude map of the  $\langle H_c \rangle$  during CR 2109-2131. Each column in the map represents the longitudinal average of  $H_c$ , at all latitudes for the indicated CR number. The blue and red colors represent the negative and positive sign of the  $H_c$  where the color scale is saturated between  $\pm 2 \times 10^{-4} G^2 m^{-1}$ . The hemispheric pattern of  $\langle H_c \rangle$ , can be seen visually by a dominance of negative (blue) in the North and positive (red) in the South hemisphere. The patches of opposite sign are also present in each hemisphere consistent with previous results that hemispheric rule is weak tendency. Nevertheless on average we find that the hemispheric rule is followed during the studied period which corresponds to the rising phase of current solar cycle 24.

For large scale fields, several researchers have used pseudo-vector reconstruction method (Pevtsov & Latushko 2000; Wang & Zhang 2010) to compute  $H_c$  and reported that the hemispheric rule is followed by large scale fields as well. Here in middle and right panels of Figure 6 we plot, respectively, the average latitudinal profile (averaged over CR 2109 to 2131) in  $0-30^\circ$  and  $>30^\circ$  latitude bands. The profile of  $H_c$  in high latitude band ( $>30^\circ$ ) is shown separately due to its relatively low amplitude. The error bars show the standard error of the mean. These profiles show that hemispheric pattern of  $\langle H_c \rangle$ , namely negative in North and positive in South, is followed in both latitude ranges quite well. Since the latitude range  $30-90^\circ$  contains mostly large scale diffuse fields, we therefore confirm the results of Pevtsov & Latushko (2000) and Wang & Zhang (2010) with observed vector magnetograms for the first time. Another feature than can be noticed from these plots is that the helicity pattern in southern hemisphere is much stronger in the sense that we see fewer patches of opposite signed helicity there, as compared to the Northern hemisphere where we see a weaker dominance of negative helicity. It is well known that the North and South hemispheres show an asymmetry in the amplitude and phase of their activity cycle. Here we show an evidence for asymmetry in the strength of hemispheric dominance of the helicity sign. Further, one can notice signatures of annual B-angle variation in the time- latitude plot in Figure 6. Such variation allows one to sample vector magnetic field at higher latitudes and therefore, study the hemispheric pattern there. We do see fluctuations in the sign of  $\langle H_c \rangle$  at high latitudes, however, the average behavior is in agreement with general hemispheric rule (Pevtsov et al. 1995).

## 6. HEMISPHERIC PATTERN FOR THE WEAK AND STRONG FIELDS

Next, we study separately the hemispheric pattern for strong and weak fields in the active region belt  $0-30^\circ$ . For segregating strong and weak field regions we used the following criterion, *Strong Fields*:  $|B_r| > 1000$  G and *Weak Fields*:  $100 < |B_r| < 500$  G. Such criterion was used by Zhang (2006) in their study of hemispheric pattern of helicity in active regions. Thus, adopting same criterion facilitates a straightforward comparison with their study. The top and bottom panels in Figure 7 show the results for strong and weak fields, respectively. The panels on the left show the time-latitude plot of  $\langle H_c \rangle$  for active region belt between  $0-30^\circ$ . Beyond  $30^\circ$  latitude only the fields weaker than 500 G remain, so we exclude these regions from comparison. The panels on the right show the latitudinal profile averaged over all 23 CRs (2109-2131) shown on the left panels. It is found that the latitudinal profile of  $H_c$  for the strong field regions follows the hemispheric tendency and the pattern is similar to one shown for  $0-30^\circ$  belt in Figure 6, for all field strengths. On the other hand for weak fields the latitudinal profile shows a weak but systematic anti-hemispheric rule, i.e., preference for positive sign of  $H_c$  in North and negative in South hemisphere. Thus, our observations which show that the strong fields obey hemispheric rule while weak fields show tendency for anti-hemispheric rule, is in disagreement with the results of Zhang (2006), who found that weak fields obey the hemispheric rule while strong fields follow anti-hemispheric rule. In another related study by Pevtsov & Longcope (2001) it was shown that the helicity of quiet sun flux obeys the hemispheric rule. During their observations many ARs were present on the Sun and the authors suggest that helicity pattern of the ARs could be reflected in the quiet sun elements simply due to the origin of quiet sun flux from decayed flux of the ARs.

## 7. DISCUSSION AND CONCLUSIONS

In this work we present for the first time synoptic (Carrington) maps of the observed vector magnetic field. These maps provide a representation of magnetic fields without any restrictive assumptions about topology of fields, and therefore, are expected to improve the outcome of coronal field extrapolation models using synoptic maps as input. Comparison of radial components derived by traditional method using LOS magnetograms with the one derived from vector data shows systematic differences in high and low-latitudes as well as in active regions. Further, we show that the non vertical nature of magnetic field leads to systematic errors in the radial field deduced from LOS observations,  $B_{r(LOS)}$ . The relative error,  $|\Delta B_r|/|B_r|$  (%) varies as tangent of the latitude and therefore becomes significant at high latitudes, even if inclination angle with respect to vertical direction remains same. The severity of the differences when using observed radial field as compared estimated radial field from LOS measurements, on the extrapolated coronal fields and solar wind derivations is presently unknown, and will be a subject of a separate future study.

As the first use for these new synoptic maps, we employed them to study the distribution of current helicity density on the Sun. We found that the hemispheric pattern of current helicity density is present during as

ending phase of cycle 24. Although the derived helicity maps do show patterns of opposite helicity present in both hemisphere, there appears to be no indication of a systematic reversal in helicity at the beginning of Cycle 24 as predicted by some previous studies (e.g., Choudhuri et al. 2004). Neither we see a presence of well-defined bands of opposite helicity co-spatial with pattern of torsional oscillations as was reported for solar cycle 22 (Pevtsov & Balasubramaniam 2003).

We studied the hemispheric pattern for weak and strong fields separately following criterion by Zhang (2006). Our results do show opposite sign of the hemispheric preference for weak and strong fields. However, opposite to Zhang (2006) we find that helicity of strong fields follow the hemispheric rule, while helicity of weak fields exhibit inverse helicity sign-hemisphere relation. Thus, for strong fields, the product of latitude ( $\theta$ ) and current helicity ( $H_c$ ) is negative in agreement with the hemispheric rule (i.e.,  $\theta \cdot H_c < 0$ ). For weak fields,  $\theta \cdot H_c > 0$ . Reasons for such disagreement between our results and those of Zhang (2006) are unknown and need further investigation.

Despite these differences the important question that remains is: why different hemispheric behavior of weak and strong fields is seen? The models of helicity generation in solar magnetic fields must be confronted with observational results. Mean field dynamo models based on  $\alpha$ -effect (Steenbeck et al. 1966; Seehafer 1996) show two helicities, the one in the mean field and another in the fluctuations. Further, both have similar magnitude but opposite sign, such that the sign of helicity in the mean and fluctuating fields is shown to be of positive and negative sign, respectively in Northern hemisphere and vice versa in Southern. In the mean field dynamo the active regions are thought of as fluctuations and not as the mean field. Thus we get same hemispheric preference for sign of observed current helicity in ARs as we get in mean field dynamo models for fluctuating field. What about the observational counterpart for helicity of the mean field? Could the mean latitudinal profile of helicity for weak fields, which shows anti-hemispheric rule, as shown in right panel of Figure 7 represent the helicity of the mean field from dynamo models, since they have same sign preference?

Another plausible explanation could be that the current helicity observed in strong and weak magnetic field are a result of two different processes. For example, helicity in strong fields of active regions could be created by  $\Sigma$ -effect (Longcope et al. 1998), while helicity of weak fields reflects their interaction with near surface flows. The twist can be induced in the magnetic flux due to vorticity of the (near) surface flows (e.g., supergranular flow, see Duvall & Gizon 2000). The (near) surface flows

(from surface to a depth of about 16 Mm) were studied using ring-diagram technique by Komm et al. (2007) as a function of magnetic flux. They found that on average, quiet regions show weakly divergent horizontal flows with small anticyclonic vorticity (clockwise in the Northern hemisphere), while locations of high activity show convergent horizontal flows with cyclonic vorticity (counterclockwise in Northern hemisphere). Consider a untwisted flux tube embedded vertically in photospheric layers and subject to clockwise horizontal flows. It can be seen that a clockwise flow will induce positive twist in magnetic flux tube and a counterclockwise flow will induce negative twist. Thus the flow patterns from local helioseismology (Komm et al. 2007) would tend to induce positive current helicity in the magnetic flux rooted in quiet regions and a negative current helicity in the magnetic flux rooted in strong field regions, in the Northern hemisphere. Such a pattern is similar to what we see in our present observations, namely a positive helicity in weak field regions and negative helicity in strong field regions in the Northern hemisphere. Thus, the observed behavior of current helicity in strong and weak fields could be explained in the framework of mean field dynamo models, or alternatively due to the interaction of magnetic flux tubes with turbulent plasma flows in the convection zone.

However, more observations are needed to improve the statistics further. Synoptic maps of vector magnetic field presented here appear to be useful tools for such statistical studies. Accumulation of more vector synoptic maps during the entire solar cycle 24 and beyond would be useful to establish patterns of helicity on the sun and will also help in testing the validity of various physical mechanism(s) that have been proposed in order to explain the hemispheric preference of magnetic twist, its associated statistical dispersion and variation with solar cycle.

We thank the anonymous referee for his/her critical comments on the manuscript. We thank Lorraine Callahan for reducing/preparing data for inversions. This work utilizes SOLIS data obtained by the NSO Integrated Synoptic Program (NISP), managed by the National Solar Observatory, which is operated by the Association of Universities for Research in Astronomy (AURA), Inc. under a cooperative agreement with the National Science Foundation. Work by SG and AAP was partially supported by NSF/SHINE Award No. 1062054 to the National Solar Observatory. GVR and SAA acknowledge support by the Ministry of Education and Science of Russian Federation (GS 8407 and GK 14.518.11.7047) and by the RFBR (12-02-31746 mol\_a, 12-02-33110 mol\_a\_ved).

*Facilities:* SOLIS (VSM).

## REFERENCES

- Abramenko, V. I., Wang, T., & Yurchishin, V. B. 1996, *Sol. Phys.*, 168, 75
- Altschuler, M. D., & Newkirk, G. 1969, *Sol. Phys.*, 9, 131
- Balasubramaniam, K. S., & Pevtsov, A. 2011, in *Society of Photo-Optical Instrumentation Engineers (SPIE) Conference Series*, Vol. 8148, Society of Photo-Optical Instrumentation Engineers (SPIE) Conference Series
- Balasubramaniam, K. S., Pevtsov, A., & Rogers, J. 2004, *ApJ*, 608, 1148
- Bao, S., & Zhang, H. 1998, *ApJ*, 496, L43
- Bao, S. D., Ai, G. X., & Zhang, H. Q. 2000, *Journal of Astrophysics and Astronomy*, 21, 303
- Canfield, R. C., Pevtsov, A. A., & McClymont, A. N. 1997, in *Astronomical Society of the Pacific Conference Series*, Vol. 111, *Magnetic Reconnection in the Solar Atmosphere*, ed. R. D. Bentley & J. T. Mariska, 341
- Choudhuri, A. R., Chatterjee, P., & Nandy, D. 2004, *ApJ*, 615, L57

- Duvall, T.L., J., & Gizon, L. 2000, *Solar Physics*, 192, 177
- Georgoulis, M. K. 2005, *ApJ*, 629, L69
- Georgoulis, M. K., Raouafi, N.-E., & Henney, C. J. 2008, in *Astronomical Society of the Pacific Conference Series*, Vol. 383, *Subsurface and Atmospheric Influences on Solar Activity*, ed. R. Howe, R. W. Komm, K. S. Balasubramaniam, & G. J. D. Petrie, 107
- Gosain, S., & Pevtsov, A. A. 2012, *Sol. Phys.*, 243
- Gosain, S., Tiwari, S. K., & Venkatakrisnan, P. 2010, *ApJ*, 720, 1281
- Hagyard, M. J., & Pevtsov, A. A. 1999, *Sol. Phys.*, 189, 25
- Hale, G. E. 1927, *Nature*, 119, 708
- Hale, G. E., Ellerman, F., Nicholson, S. B., & Joy, A. H. 1919, *ApJ*, 49, 153
- Hao, J., & Zhang, M. 2011, *ApJ*, 733, L27
- Harvey, J., Gillespie, B., Miedaner, P., & Slaughter, C. 1980, *NASA STI/Recon Technical Report N*, 81, 21003
- Henney, C. J., Keller, C. U., & Harvey, J. W. 2006, in *Astronomical Society of the Pacific Conference Series*, Vol. 358, *Astronomical Society of the Pacific Conference Series*, ed. R. Casini & B. W. Lites, 92
- Howe, R., Christensen-Dalsgaard, J., Hill, F., Komm, R. W., Larsen, R. M., Schou, J., Thompson, M. J., & Toomre, J. 2000, *ApJ*, 533, L163
- Jones, H. P., Harvey, J. W., Henney, C. J., Hill, F., & Keller, C. U. 2002, in *ESA Special Publication*, Vol. 505, *SOLMAG 2002. Proceedings of the Magnetic Coupling of the Solar Atmosphere Euroconference*, ed. H. Sawaya-Lacoste, 15–18
- Keller, C. U., Harvey, J. W., & Giampapa, M. S. 2003, in *Society of Photo-Optical Instrumentation Engineers (SPIE) Conference Series*, Vol. 4853, *Society of Photo-Optical Instrumentation Engineers (SPIE) Conference Series*, ed. S. L. Keil & S. V. Avakyan, 194–204
- Komm, R., Howe, R., Hill, F., Miesch, M., Haber, D., & Hindman, B. 2007, *ApJ*, 667, 571
- Longcope, D. W., Fisher, G. H., & Pevtsov, A. A. 1998, *ApJ*, 507, 417
- Martin, S. F., Lin, Y., & Engvold, O. 2008, *Sol. Phys.*, 250, 31
- Metcalf, T. R., Jiao, L., McClymont, A. N., Canfield, R. C., & Uitenbroek, H. 1995, *ApJ*, 439, 474
- Petrie, G. J. D., & Patrikeeva, I. 2009, *ApJ*, 699, 871
- Pevtsov, A. A., & Balasubramaniam, K. S. 2003, *Advances in Space Research*, 32, 1867
- Pevtsov, A. A., & Canfield, R. C. 1998, in *Astrophysics and Space Science Library*, Vol. 229, *Observational Plasma Astrophysics : Five Years of YOHKOH and Beyond*, ed. T. Watanabe & T. Kosugi, 85
- Pevtsov, A. A., Canfield, R. C., & Latushko, S. M. 2001, *ApJ*, 549, L261
- Pevtsov, A. A., Canfield, R. C., & Metcalf, T. R. 1994, *ApJ*, 425, L117
- , 1995, *ApJ*, 440, L109
- Pevtsov, A. A., & Latushko, S. M. 2000, *ApJ*, 528, 999
- Pevtsov, A. A., & Longcope, D. W. 2001, in *Astronomical Society of the Pacific Conference Series*, Vol. 236, *Advanced Solar Polarimetry – Theory, Observation, and Instrumentation*, ed. M. Sigwarth, 423
- Pevtsov, A. A., & Peregud, N. L. 1990, in *Washington DC American Geophysical Union Geophysical Monograph Series*, Vol. 58, *Physics of Magnetic Flux Ropes*, ed. C. T. Russel, E. R. Priest, & L. L. C., 161–165
- Priest, E. R. 1984, *Solar magneto-hydrodynamics*
- Richardson, R. S. 1941, *ApJ*, 93, 24
- Rudenko, G. V., & Anfinogentov, S. A. 2011, *ArXiv e-prints*
- Rust, D. M. 1999, in *Washington DC American Geophysical Union Geophysical Monograph Series*, Vol. 111, *Magnetic Helicity in Space and Laboratory Plasmas*, ed. M. R. Brown, C. R. C., & P. A. A., 221
- Rust, D. M., & Kumar, A. 1996, *ApJ*, 464, L199
- Schou, J., et al. 2012, *Sol. Phys.*, 275, 229
- Seehafer, N. 1990, *Sol. Phys.*, 125, 219
- , 1996, *Phys. Rev. E*, 53, 1283
- Skumanich, A., & Lites, B. W. 1987, *ApJ*, 322, 473
- Smith, C. W. 1999, in *Washington DC American Geophysical Union Geophysical Monograph Series*, Vol. 111, *Magnetic Helicity in Space and Laboratory Plasmas*, ed. M. R. Brown, C. R. C., & P. A. A., 239
- Steenbeck, M., Krause, F., & Rädler, K.-H. 1966, *Zeitschrift Naturforschung Teil A*, 21, 369
- Su, J. T., Sakurai, T., Suematsu, Y., Hagino, M., & Liu, Y. 2009, *ApJ*, 697, L103
- Tadesse, T., Wiegmann, T., Inhester, B., MacNeice, P., Pevtsov, A., & Sun, X. 2013, *A&A*, 550, A14
- Wang, C., & Zhang, M. 2010, *ApJ*, 720, 632
- Yeates, A. R., Mackay, D. H., & van Ballegooijen, A. A. 2008, *ApJ*, 680, L165
- Zhang, M. 2006, *ApJ*, 646, L85

## APPENDIX

EFFECT OF NOISE ON  $\Delta B_R/|B_R|$ 

Let us assume that  $B_r$  and  $B_r(LOS)$  (or simply  $B_L$ ) have same sign (say positive), and noise ( $\sigma$ ) is small compared to magnitude of radial field (both  $B_r$  and  $B_L$ )

Then,

$$\frac{\Delta B_r}{|B_r|} = \frac{|B_r \pm \sigma| - |B_L \pm \sigma|}{|B_r \pm \sigma|} = \frac{(B_r \pm \sigma) - (B_L \pm \sigma)}{B_r \pm \sigma} = \frac{(B_r - B_L) \pm \sigma}{B_r \pm \sigma}$$

If  $\sigma \ll B_r$  and  $B_r \approx B_L$ , we can re-write the above as

$$\frac{(B_r - B_L) \pm \sigma}{B_r \pm \sigma} \approx \frac{\pm \sigma}{B_r}$$

Thus, as noise ( $\sigma$ ) increases, the scatter in the relative difference,  $\Delta B_r/|B_r|$ , also increases proportionally. A systematic latitudinal pattern in the sign of relative difference,  $\Delta B_r/|B_r|$ , as seen in top panel of Figure 3 is not expected from random noise in  $B_r$  and  $B_L$ .



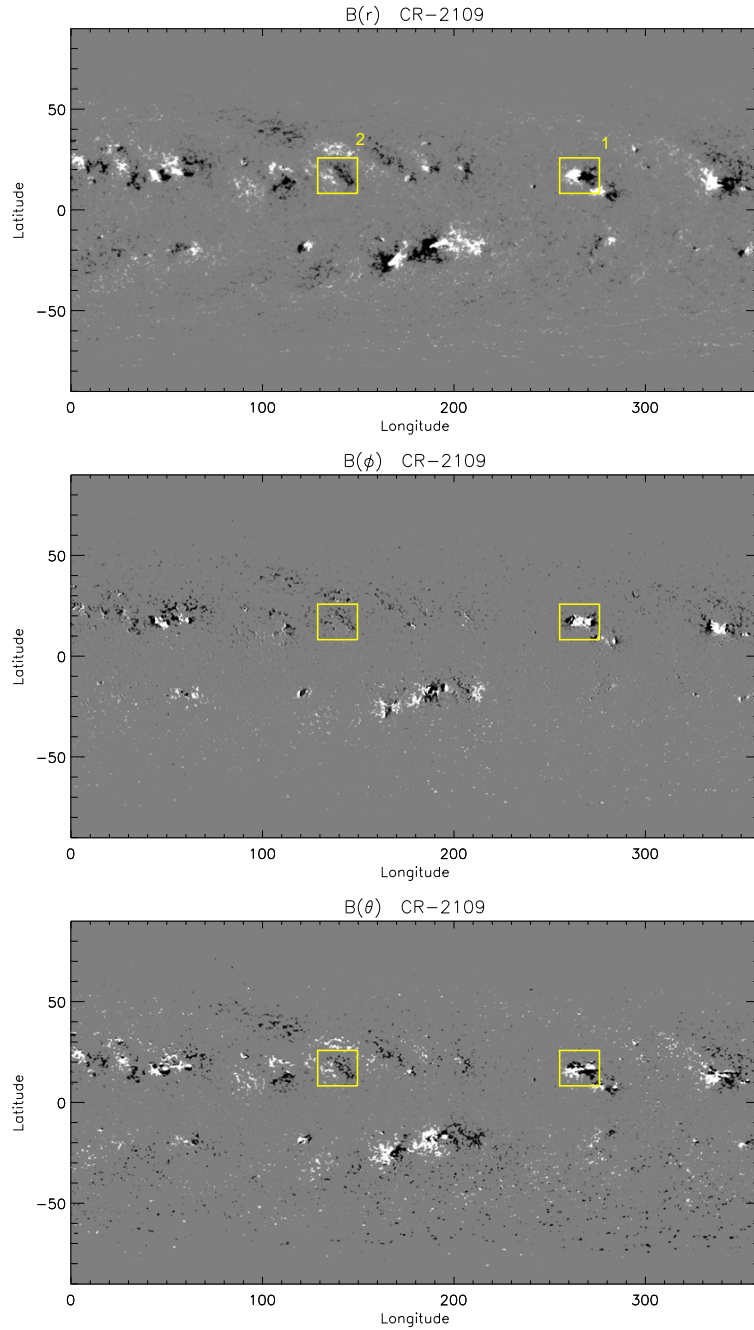


FIG. 1.— Synoptic Carrington map of the vector magnetic field components synthesized using full disk SOLIS/VSM vector magnetograms is shown for CR-2109. The panels from top to bottom show the distribution of  $B(r)$ ,  $B(\theta)$  and  $B(\phi)$  components, respectively. The  $B_r$  map is scaled between  $\pm 100$  G and  $B_\theta$  and  $B_\phi$  maps are scaled to  $\pm 20$  G. The positive values of  $B_r$ ,  $B_\theta$  and  $B_\phi$  points respectively, upwards, Southwards and to the right (Westward). The zoom-in of the regions marked by rectangles ‘1’ and ‘2’ is shown in Figure 2.

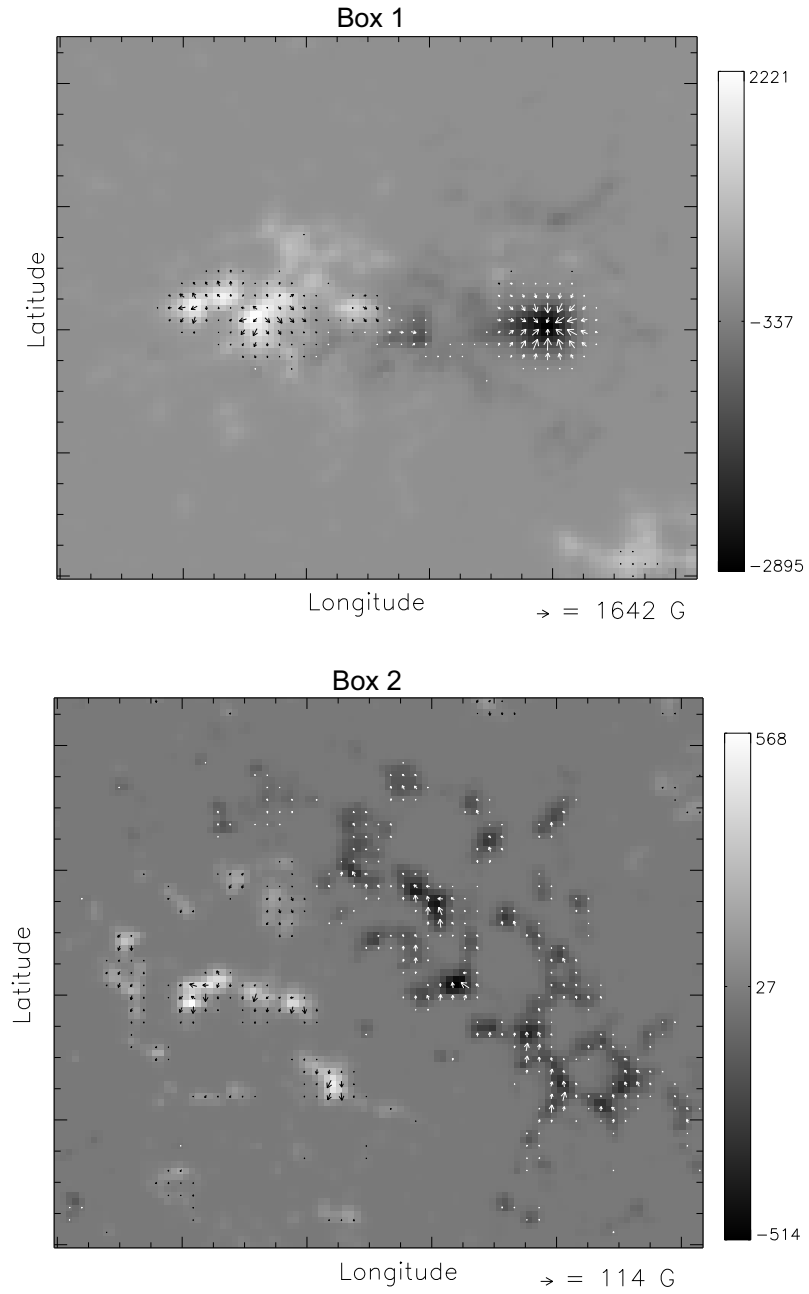


FIG. 2.— The zoom-in of the two regions marked by rectangles, ‘1’ and ‘2’, in Figure 1 is shown. The arrow at the bottom and color bar on the side of the panels show scale of transverse and radial field, respectively. The tick-marks on the latitude and longitude axis represent 1 degree increments.

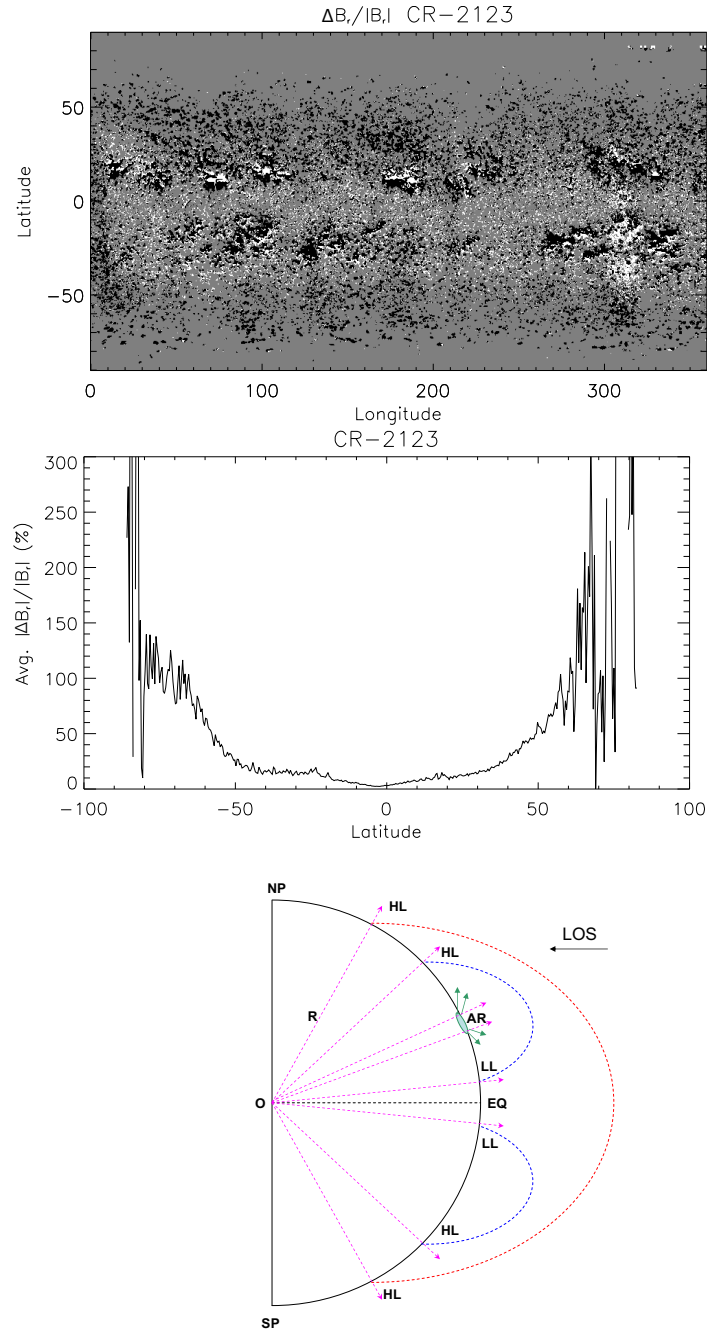


FIG. 3.— Top panel displays the signed relative difference,  $\Delta B_r/|B_r|$  (%), between the absolute values of observed radial field,  $|B_r|$ , and the radial field derived from LOS magnetic field,  $|B_r(LOS)|$ , during Carrington rotation 2123. The signed relative difference is saturated between  $\pm 5\%$  to emphasize the sign of the difference. The middle panel shows the longitudinal average of absolute relative difference,  $|\Delta B_r|/|B_r|$  (%). In the bottom panel we show a cartoon model to illustrate the sign pattern observed in the top panel.

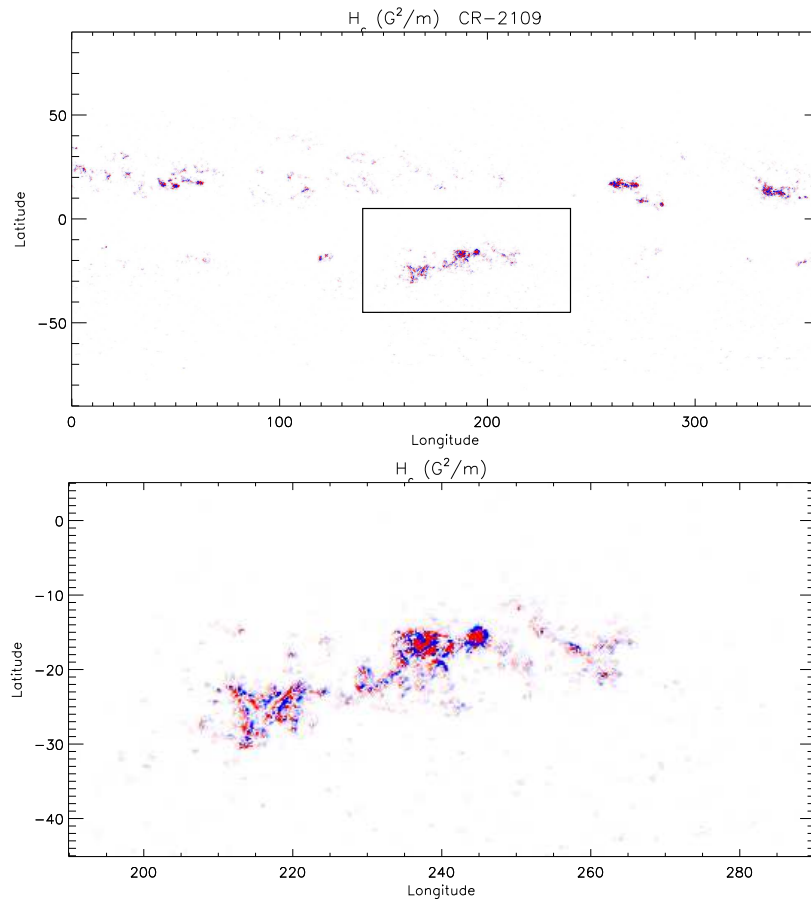


FIG. 4.— Synoptic map of current helicity density,  $H_c$ , is shown in the top panel for CR 2109. The rectangular region marked in the map is zoomed and displayed in the lower panel. The amplitude of  $H_c$  in the displayed images is scaled between  $\pm 2 \times 10^{-3} \text{ G}^2 \text{ m}^{-1}$ .

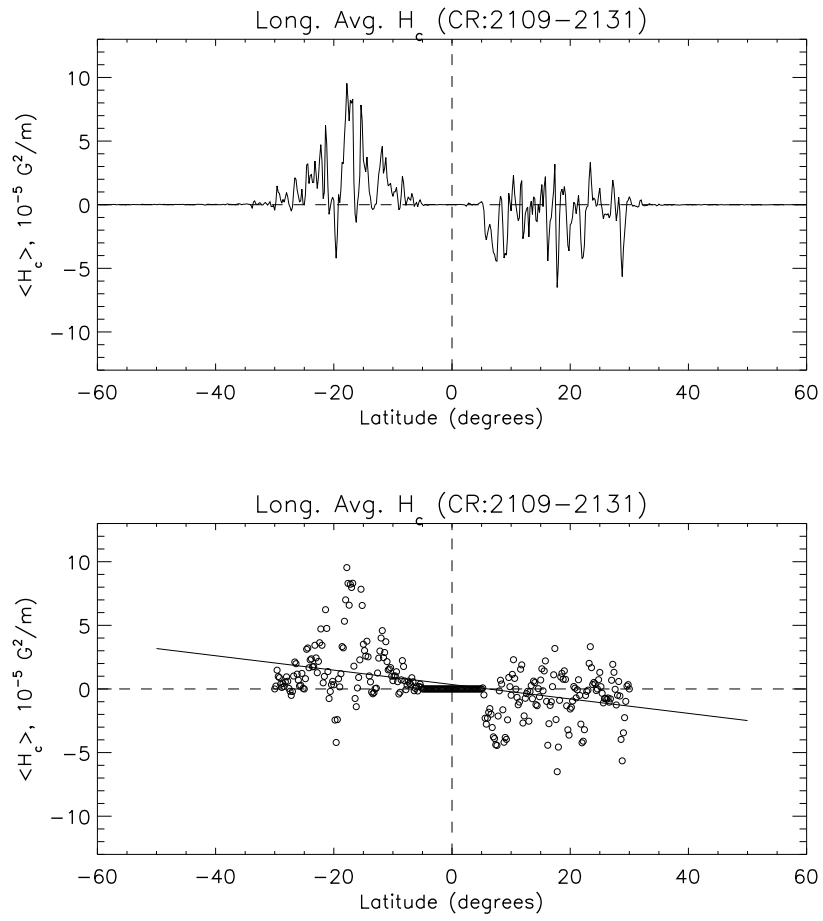


FIG. 5.— The top panel shows longitudinal averaged profile of  $H_c$  over all CRs (2109 to 2131). The bottom panel shows the same profile between  $0\text{-}30^\circ$  along with a linear fit with a negative slope.

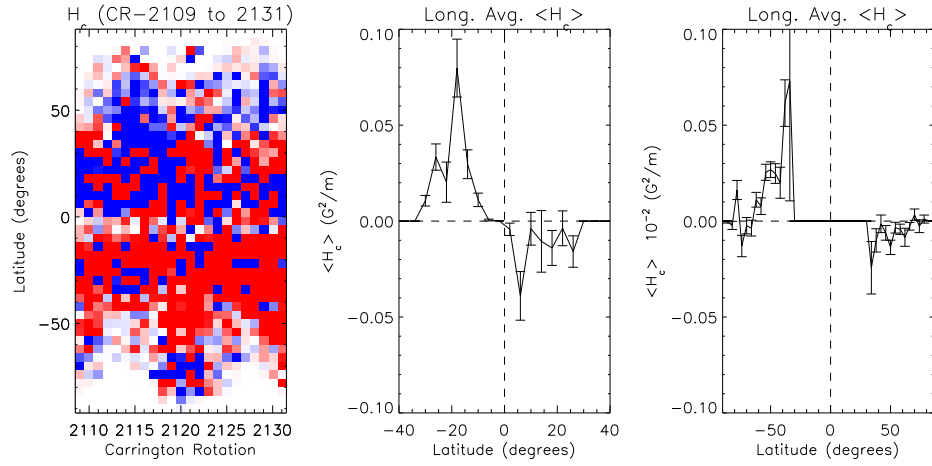


FIG. 6.— Left panel shows the time-latitude plot of current helicity density,  $H_c$ . Each column corresponds to the longitude average of  $H_c$  for the Carrington rotation and re-binned into  $4^\circ$  latitude bins. The blue (red) color represents the negative (positive) sign of  $H_c$ . The magnitude of  $H_c$  is scaled between  $\pm 2 \times 10^{-4} \text{ G}^2 \text{ m}^{-1}$ . The middle and right panels show the mean latitudinal profile of  $H_c$  (derived from time-latitude plot on left) over  $0\text{-}30^\circ$  and  $30\text{-}90^\circ$ , respectively. The error bars show the standard error of the average  $H_c$  value.

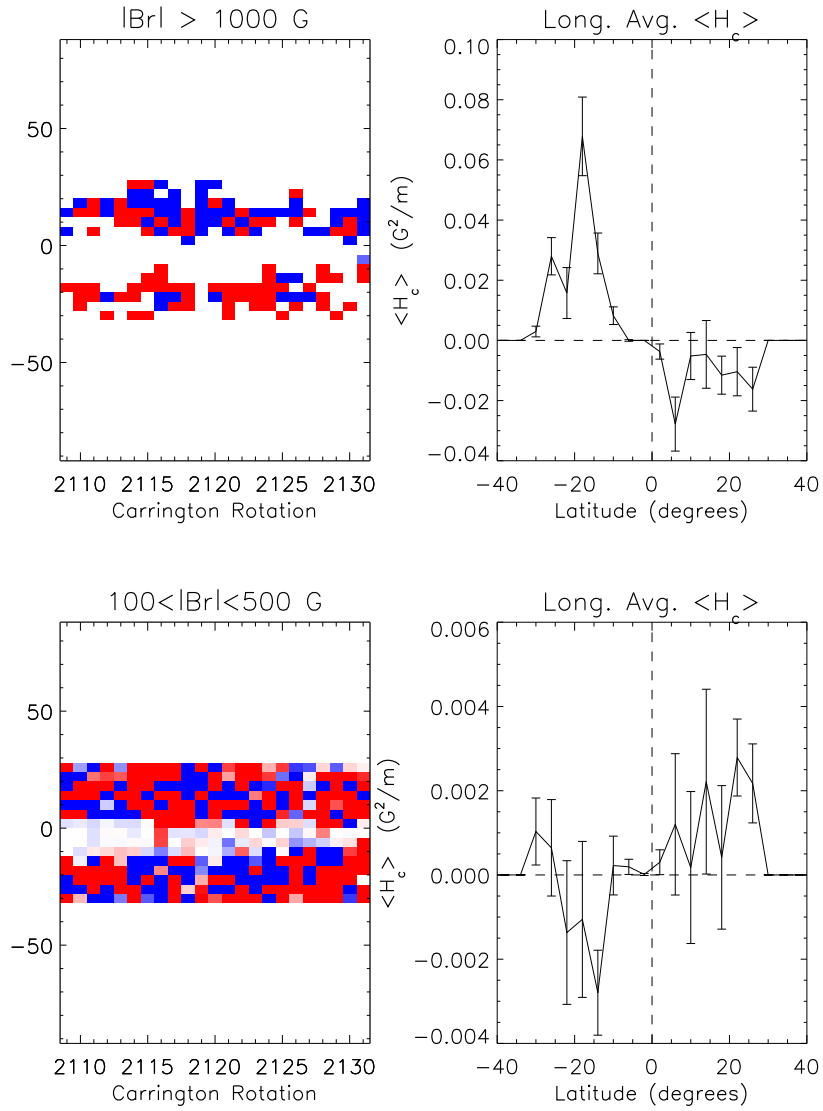


FIG. 7.— Left top (bottom) panels show the time-latitude plot of current helicity density,  $H_c$  for strong (weak) fields over  $0-30^\circ$  latitude belt. Each column corresponds to the longitude average of  $H_c$  for the Carrington rotation as labeled. The blue (red) color represents the negative (positive) sign of  $H_c$ . The magnitude of  $H_c$  is scaled between  $\pm 5 \times 10^{-4} G^2 m^{-1}$ . The right panels (both top and bottom row) show the mean latitudinal profile of  $H_c$ , derived from respective time-latitude plots on the left. The error bars show the standard error of the average  $H_c$  value.